Heterogeneous reaction kinetics of a perovskite oxygen carrier determined by MFB-TGA for chemical looping combustion coupled with oxygen uncoupling

Lei Liu[a], Zhenshan Li*[a], Zuoan Li[b], Yngve Larring[b], Ningsheng Cai[a]

a. Key Laboratory for Thermal Science and Power Engineering of Ministry of Education, Department of Energy and Power Engineering, Tsinghua University, Beijing 100084, China

b. SINTEF Industry, Sustainable Energy Technology, P.O. Box 124 Blindern, NO-0314 Oslo, Norway

*Corresponding Author

Telephone number: +86-10-62789955

E-mail address: lizs@mail.tsinghua.edu.cn

Abstract

The chemical looping oxygen uncoupling (CLOU) technology is based on oxygen carrier releasing gaseous O_2 to combust the fuel. The determination of more exact heterogeneous kinetics of oxygen release from oxygen carriers is a crucial task for modelling, used to predict performance and design of demonstrating pilot units. Thermogravimetric analysis (TGA) is the most widely used method to measure the kinetics. However, the mass and heat transfer limitations observed inside the TGA specially for CLOU effect will lead to underestimation of the kinetics. Micro-fluidized bed thermogravimetric analysis method (MFB-TGA) solve this challenge to measure the fast heterogeneous oxygen release kinetics precisely, based on real-time mass measurement of oxygen carrier in a fluidizing state with similar mass and heat transfer characteristics as in a CLC reactor. In this study the oxygen uncoupling kinetics and redox reactions kinetics of a newly developed

perovskite oxygen carrier material ($CaMn_{0.5}Ti_{0.375}Fe_{0.125}O_{3-\delta}$) is established using a MFB-TGA method. It is found that the oxygen uncoupling kinetics measured by MFB-TGA is obviously faster than that measured by regular TGA Q500. The rate of oxygen uncoupling is enhanced with the increase in temperature. An interesting finding is that the oxidization reaction of $CaMn_{0.5}Ti_{0.375}Fe_{0.125}O_{3-\delta}$ occurs only in the initial stage controlled by chemical reaction, and the time required for full oxidation is ~ 5 s, while the reduction kinetics consists of a fast reaction stage and a slow reaction stage, controlled by chemical reaction at low conversion level and diffusion through the product layer at high conversion level, respectively. Both the oxygen uncoupling kinetic parameters and redox kinetic parameters are obtained by analyzing the MFB-TGA data based on the simplified K-L model for the fluidized bed. The morphology characterizations of the fresh and tested $CaMn_{0.5}Ti_{0.375}Fe_{0.125}O_{3-\delta}$ particles were investigated by SEM-EDS. The comparison of heterogeneous reaction kinetics with the mainstream OCMs were done.

Key words: Chemical looping combustion; Oxygen uncoupling; Oxygen carrier; Perovskite; Kinetics; MFB-TGA

Highlights:

- A new perovskite oxide, $CaMn_{0.5}Ti_{0.375}Fe_{0.125}O_{3-\delta}$, was developed as oxygen carrier.

- Micro-fluidized bed thermogravimetric analysis (MFB-TGA) was used for kinetic study.

- Oxygen uncoupling kinetics was accurately measured by MFB-TGA.

- Full oxidation can be achieved within 5 s.

1. Introduction

Chemical Looping Combustion (CLC) is an alternative technology for reducing the economic and energy costs associated with the CO_2 capture from the fossil fuel conversion processes [1]. A

CLC unit consists of two interconnected fluidized bed reactors, where one is the air reactor and the other is the fuel reactor, using a metal-based oxygen carrier material (OCM) to transfer the required oxygen between the two reactors for fuel conversion. Chemical Looping with Oxygen Uncoupling (CLOU), proposed by Lyngfelt et al. [2], takes the advantages of an oxygen carrier which is capable of releasing gaseous O_2 in inert atmospheres to combust the fuel in the fuel reactor. CLOU is thought to be a particularly suitable method for solid fuels, such as coal, petroleum coke, and biomass, since a full conversion can be achieved if sufficient OC is present [2,3]. Oxides, based on Cu- [4], Mn- [5] and Co- [6], are frequently proposed as the OCMs in the CLOU, since these materials have suitable thermodynamics for O_2 release under an inert atmosphere. [7]. However, stability could be an issue for transition metal oxides due to phase change during redox cycles. An OCM must possess high oxygen transfer capacity, suitable reactivity and adequate thermodynamics, physical strength and stable performance in many redox cycles, and being cost effective and environmentally friendly.

Perovskite-type complex oxides (formula as ABO_3) are normally stable over a very large range of oxygen partial pressures and known for its low cation diffusion compared to oxygen ionic diffusion. In addition, the crystal lattice can accommodate significant changes in oxygen content through generation and annihilation of oxygen vacancies. These properties of good oxygen transport and exchange without undergoing crystal phase changes are not possessed to an appreciable degree by transition metal oxides as mentioned above, and are making perovskite oxides possessing such properties promising as OCMs [8,9]. $CaMnO_{3-\delta}$ has shown high reactivity with gas fuels and also thermodynamic properties for oxygen uncoupling [8-10]. In this regard, $CaMnO_{3-\delta}$ can be considered as a promising OCM for CLOU with solid fuels. Doping Ti on B-sites normally increases the stability, while Fe-doping can enhance its catalytic ability [11]. The $CaMn_{1-x-y}Ti_xFe_yO_{3-\delta}$ series

of OCMs were investigated with regards to structure stability and oxygen transport properties [12,13]. In the present contribution, the composition $CaMn_{0.5}Ti_{0.375}Fe_{0.125}O_{3-\delta}$, was designed for a balance between the oxygen transfer capacity in CLOU (Mn-rich), stability (certain amount of Ti) and reactivity (Fe addition).

Heterogeneous reactions kinetics of oxygen uncoupling and reduction/oxidation play important roles in material development, reactor design and process demonstration and optimization. Therefore, it is highly required for the accurate kinetic determination of the $CaMn_{0.5}Ti_{0.375}Fe_{0.125}O_{3-\delta}$ oxygen carrier. Thermogravimetric analysis (TGA) and fluidized bed reactor tare commonly used methods available for the determination of oxidization and reduction kinetics of OCMs. Researchers from ICB-CSIC Spain [10,14,15], Utah America [16] and Cambridge Britain [4] used TGA to determine the oxygen uncoupling kinetics of OCMs. An unavoidable operation in CLOU experiment is the switch between the oxidation step and oxygen uncoupling step by switching the air stream to pure inert gas such as nitrogen or argon, and the gas phase O_2 will be released from oxygen carrier to the atmosphere of pure inert gas. However, such a switch procedure cannot immediately empty all oxygen contents inside TGA chamber, leading to a gradual decrease in the concentration of O_2. This gradual replacement of O_2 by pure inert gas will inevitably affect the kinetics measurement of oxygen uncoupling because the O_2 concentration around the OCM particles has a hindering effect on the driving force of oxygen uncoupling reaction. Therefore, the kinetics will be underestimated due to the mass and heat transfer limitations inside TGA [17]. The oxygen uncoupling kinetics can also be measured by the fluidized bed reactor method which is based on the concentration signal of the tail gas [18,19]. However, the effect of an imperfect plug flow and the fluctuation of the gas concentration signal due to gas switch cannot be avoided [20]. Although

deconvolution method was proposed to correct the gas signal, the deconvolution method may not minimize the negative influence of the plug flow and axial mixing in case of a fast oxidation reaction [18]. The accurate kinetic measurement of oxygen uncoupling is still a challenge, and there is an ongoing need to develop an experimental technique for fast oxygen uncoupling kinetics

In the present contribution, we addressed fast redox kinetics with a newly developed micro fluidized bed thermogravimetric analysis (MFB-TGA) method which is based on the real-time measurement of mass signals [21]. Due to significantly enhanced mass and heat transfer in the fluidizing state, the measured reaction rate is faster for different gas-solid reactions as compared to that determined with regular TGA apparatus, such as the redox kinetics of oxygen carrier materials [21,22], gasification of a lignite [23] and carbonation of CaO [24]. The main objective of this work was to determine the oxygen uncoupling and redox kinetics of a newly developed perovskite $CaMn_{0.5}Ti_{0.375}Fe_{0.125}O_{3-\delta}$, using the micro-fluidized bed thermogravimetric analysis (MFB-TGA) technology. The experimental data of MFB-TGA were analyzed by a two-stage kinetic model coupled with K-L two phase fluidized bed reactor model. The reaction rates of oxygen uncoupling determined by the MFB-TGA were also compared with those from a regular TGA.

2. Experimental

2.1. Oxygen carrier material

Perovskite $CaMn_{0.5}Ti_{0.375}Fe_{0.125}O_{3-\delta}$ powders were fabricated by means of spray granulation using commercial Mn_3O_4 and Fe_2O_3, together with the corresponding stoichiometric amounts of $CaCO_3$, and TiO_2 as the starting ingredients. To obtain oxygen carrier particles with sufficient mechanical strength and with the desired crystalline phases, sintering was performed in air at 1350 °C for 12 h. According to the X-ray Fluorescence (XRF) results, the OCM was composed of

40.82 wt.% CaO, 19.16 wt.% TiO$_2$, 29.06 wt.% MnO and 8.27 wt.% Fe$_2$O$_3$. A particle size ranging

from 180 to 250 μm was selected to determine the reaction kinetics. More properties of the OCM

particles are listed in Table 1. The oxygen transport capacity was determined by both

thermochemical and experimental results, see sections below.

Table 1 Physical properties of the CaMn$_{0.5}$Ti$_{0.375}$Fe$_{0.125}$O$_{3-\delta}$ oxygen carrier

d_p(μm)	ρ_s(kg/m^3)	Porosity	BET(m^2/g)	$u_{t,OC}$ (m/s)	$c_{p,OC}$ (J/kg/K)
180-250	2854	0.48	0.21	1.08[1]	940

[1] terminal velocity was calculated at 900 ^{o}C in CO$_2$ atmosphere [25]

2.2. Regular TGA experiment

A commercial thermogravimetric analyzer (Q500, TA Instruments) was used in this experiment.

In the regular TGA experiment, to reduce the impact of produced O$_2$ on the oxygen uncoupling

processes, ~ 15 mg sample was added to an alumina crucible. The alumina crucible is very shallow

(height: 1 mm, diameter: 10 mm), and the OCM particles are dispersed in it, to avoid a packed state.

The gas flowrate injected to in Q500 is 100 ml/min (at 273.15 K and 1 bar) along horizontal direction.

In a typical experiment, the sample was heated under a 21 vol.% O$_2$ agent at a heating rate of 20

K/min to 900 ^{o}C. When the mass became stable, pure N$_2$ was injected and isothermal oxygen

uncoupling reaction began.

2.3. Micro-fluidized bed thermogravimetric analysis (MFB-TGA)

A micro-fluidized bed fluidized bed thermogravimetric analysis apparatus (MFB-TGA) was

applied to investigate the kinetics of oxygen uncoupling and redox reaction of the OCM particles.

The apparatus mainly consists of an electric heating furnace, a fluidized bed reactor with bubbling

state, a gas supply system and a measuring system, see Fig. 1(a). The reactor (I.D. 30 mm) is made

by quartz, and the gas distributor is a porous quartz plate. The flowrates of fluidizing agents were

controlled by well calibrated mass flowmeters. The gas flowed into the bottom of the micro-

fluidized bed reactor through switching well-connected magnetic valves. A mass transducer with a measurement accuracy of 1 mg was applied to measure the whole weight including the reactor and bed materials. A K-type thermocouple enclosed in the reactor was used to record bed temperature above the gas distributor. A differential pressure sensor was installed to measure the pressure difference between the gas inlet and outlet. The measurement error of the MFB-TGA is within ±1 mg, which guarantees that the mass change is mainly caused by gas-solid reaction between samples and gas phases [21]. More details about this technique can be found elsewhere [21-24].
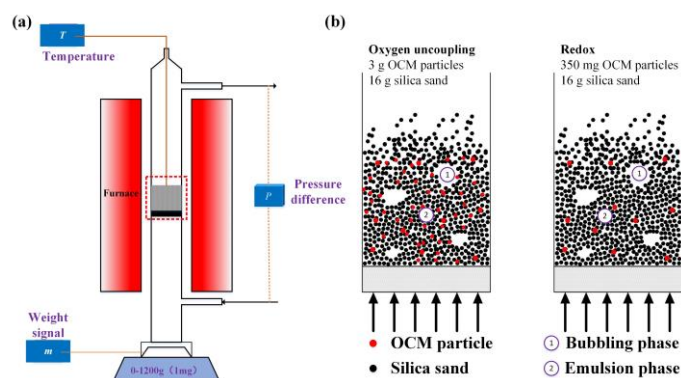

Fig. 1. Schematic diagrams of (a) the MFB-TGA apparatus and (b) the solid particles in the

bubbling bed reactor

The kinetics of oxygen uncoupling and redox reaction were obtained at isothermal conditions in the MFB-TGA apparatus. For a typical test of oxygen uncoupling reaction, $\sim$ 16 g silica sand (black color particles in Fig.1(b)) was firstly filled as the bed material and $\sim$ 3 g fully oxidized OCM particles (red color particles in Fig.1(b)) were added into the reactor after heating up to 800-930 °C under a 21 vol.% O_2 fluidizing agent, as shown in Fig. 1(b). When the stability of mass and temperature signals were obtained, 3 isothermal cycles of O_2 release and uptake were conducted by switching the fluidizing agents between 100 vol.% N_2 and 21 vol.% O_2. After that, 6 redox cycles were conducted by altering the fluidizing gases between 10 vol.% H_2 and 21 vol.% O_2. These cycles

were used to remove initial effect, since the perovskite do not need activation like many minerals. Then, there were also several cycles in which 100 vol.% N_2 was used as a fluidizing gas, in order to evaluate the oxygen uncoupling kinetics in an inert atmosphere. For the determination of redox kinetics, ~ 16 g silica sand was also filled as the bed material but the fully oxidized OCM mass added into the reactor is only ~ 350 mg after heating up to 700-900 °C, in order to minimize the influence of gas diffusion, as shown in Fig. 1(b). During the heating stage, a 21 vol.% O_2 was acted as the fluidizing agent. Afterwards, isothermal cycles of reduction and oxidization reaction were conducted by alternating the fluidizing agents between 21 vol.% O_2 and 10 vol.% H_2, or 21 vol.% O_2 and 10 vol.% CH_4. Pure N_2 was introduced for 30 s in-between to prevent mixing of the reducing and oxidizing gases. Table 2 shows the experimental scheme of kinetics determination of oxygen uncoupling and redox reactions. Previous researches have proven that the reduction and oxidization of OCMs are usually first order [5,15,21]. Therefore, the effect of gas concentrations on the reduction and oxidation rate was not evaluated. The fluidizing gas flowrates were 1.2-1.5 NL/min for testing at different temperatures, corresponding a superficial velocity of 3-5 U_{mf}. Each redox cycle was repeated at least 3 times to ensure reproducibility.

In order to eliminate the noise when gases are introduced and switched, all balance gases in the reaction gases were well selected to ensure that reaction gases and inert gas (N_2) have similar densities, see the supplementary material. For example, 21.76 vol. % Ar and 3.5 vol. % He mixed with N_2 were serviced as the balance gases of 10 vol.% H_2 and 21 vol.% O_2 in order to keep the stability of mass signals. The effect of gas switch on mass signals could be ignored, as shown in Fig. 2. Therefore, the real-time mass change was induced by the heterogeneous reactions rather than background of the setup.

Table 2 Experimental conditions for determining the heterogeneous reactions kinetics

	Temperature	Fluidizing agents	Periods	No of cycles
Oxygen		O_2/N_2	300s/60s	3
uncoupling	800-930 °C	$O_2/N_2/H_2$	60s/30s/8min	6
reaction		O_2/N_2	300s/60s	>3
Redox reaction I	700-900 °C	$O_2/N_2/H_2$	60-120s/30s/60-240s	>3
Redox reaction II	800-900 °C	$O_2/N_2/CH_4$	60s/30s/300s	>3
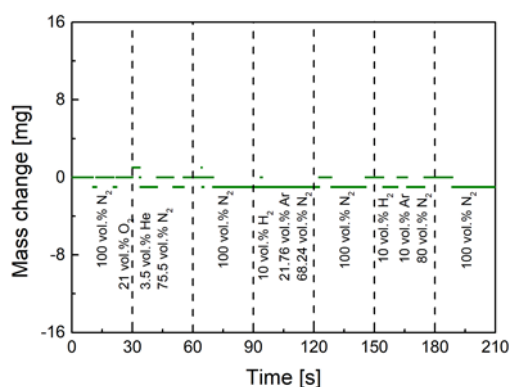
Fig. 2. The mass change between the gases switch at 900 °C (Only 16.35 g silica sand was filled)

2.4. Data evaluation

For the fresh and tested $CaMn_{0.5}Ti_{0.375}Fe_{0.125}O_{3-\delta}$ particles, the morphology properties of the particles surface and cross section were analyzed using a scanning electron microscope (Zeiss Merlin, 0.8nm@15kV) coupled with an energy dispersive spectrometer (EDS, 124eV@ B4~U92). The cross section was finally polished using a diamond polishing paste with 1.5 μm prior to SEM-EDS characterization.

The mass transducer recorded the real-time mass signal, $m(t)$, during the experiments. The oxygen transport capacity for oxygen uncoupling ($R_{oc,ou}$) was theoretically calculated as below, and

the total oxygen transport capacity ($R_{oc,t}$) was determined by the experimental results. For the oxygen uncoupling reaction, 3 g OCM particles in full oxidization state was added in the reactor (m_{oc}=3 g). The whole mass (m_o), including the quartz reactor, 16 g silica sand and 3 g sample, was 671.075 g at the initial state, as see Fig. 3(a). Once the fluidizing agent was switched to N_2, the real-time mass, $m(t)$, decreased due to O_2 release. The conversion level can be described as Eq. (1).

$$X_{ou}(t)=\frac{m_o-m(t)}{R_{oc,ou}m_{oc}}$$
(1)

Different from the oxygen uncoupling tests, the redox kinetics were determined using 16 g silica sand and 350 mg OCM particles as bed materials, as illustrated in Fig. 1(b). For the redox reactions, the whole mass change caused by gas-solid reaction is corresponding to the total oxygen transport capacity ($R_{oc,t}$), the value of which is far higher than that of the oxygen transport capacity for oxygen uncoupling ($R_{oc,ou}$). Hence 350 mg samples are enough, which brings a mass change of 19 mg for the redox test, see below. For a typical test, the whole mass was 668.257 g, including the 0.35 g sample in full oxidization state, prior to reaction with H_2, as see Fig. 3(b). The decrease in the real-time mass, $m(t)$, was caused by reduction with H_2. After all the active lattice oxygen was used up, the whole mass was decreased to 668.238 g. Since all the OCM particles were in full reduction state in this situation, the value of m_r was 668.238 g. The mass loss in the reduction stage was entirely regenerated after introducing air agent, as shown by the increase in the real-time mass, $m(t)$. The conversion levels were described as Eqs. (2) and (3) for the reduction (X_r) and oxidation (X_o) reactions, respectively. The numerator in below equations describes the mass change induced by the heterogeneous reactions.

$$X_r(t)=\frac{m_o-m(t)}{R_{o,t}m_{oc}}$$
(2)

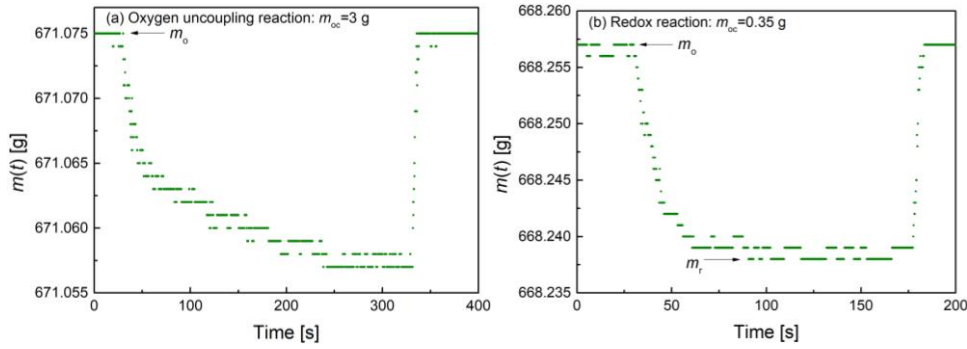$$X_o(t) = \frac{m(t) - m_r}{R_{o,t} m_{oc}}$$ (3)

Fig. 3. Mass signals during (a) oxygen uncoupling and (b) redox reactions with O_2/H_2 at 900 °C

3. Models

3.1. Thermochemical calculations

The chemical formula of the OCM material is $CaMn_{0.5}Ti_{0.375}Fe_{0.125}O_{3-\delta}$. Due to the absence of

available thermodynamical data, it is reasonable to assume that the thermodynamic parameters of

$CaMnO_{3-\delta'}$ can be used for calculation [8], considering $CaMn_{0.5}Ti_{0.375}Fe_{0.125}O_{3-\delta}$ is equivalent to

$(CaMnO_{3-\delta'})_{0.5}(CaTiO_3)_{0.375}(CaFeO_3)_{0.125}$. Leonidova et al. [8] reported a phase diagram for

$CaMnO_{3-\delta'}$, and the oxygen vacancy (δ') for the $CaMnO_{3-\delta'}$ perovskite depends on the partial pressure

of O_2 and temperature. Eq. (4) was proposed to calculate δ' values as a function of temperature, and

the equilibrium O_2 concentration ($C_{O_2,eq}$) is a function of the temperature and the oxygen vacancy,

as described by Eq. (5) [8,15]. The evaluated equilibrium O_2 concentration ($C_{O_2,eq}$) is used to model

calculation for oxygen uncoupling and oxidization reaction, as seen in Section 3.

$$3\text{-}\delta' = \min\left\{3, d_1 + c_1 T^{-1} + b_1 T^{-2} + a_1 T^{-3}\right\}$$ (4)

$$C_{O_2,eq} = \frac{101325}{R_g T} \exp\left[M + \frac{N}{T}\right]$$ (5)

where T is the reaction temperature in Kelvin, R_g (J/mol/K) is the gas constant, and M and N

coefficients are calculated as a function of (3-δ'), see Eqs. (6) and (7). The coefficients for Eqs. (4),

(6) and (7) are showed in Table 3.

$$M = d_2 + c_2\left(3\text{-}\delta'\right) + b_2\left(3\text{-}\delta'\right)^2 + a_2\left(3\text{-}\delta'\right)^3 \tag{6}$$

$$N = d_3 + c_3\left(3\text{-}\delta'\right) + b_3\left(3\text{-}\delta'\right)^2 + a_3\left(3\text{-}\delta'\right)^3 \tag{7}$$

Table 3 Coefficients of equations in this section (All digits are necessary to obtain accurate results)

	a_i	b_i	c_i	d_i
Eq. (4)	1889400000	-7223100	8739.3	-0.40395
Eq. (6)	-62863.581	554138.87	-1627925	1593883.5
Eq. (7)	82355555	-725574860	2130535800	-2085079400

In this work, two different oxygen transport capacities are defined: (1) $R_{OC,t}$: describes the total fraction of oxygen which can be transferred to fuel; (2) $R_{OC,ou}$: describes fraction of O_2 which can be released through the oxygen uncoupling reaction in inert atmosphere. According to Leonidova et al., these two oxygen transport capacities can be determined by thermochemical calculations [8]. The $R_{OC,t}$ depends the parameter δ'.
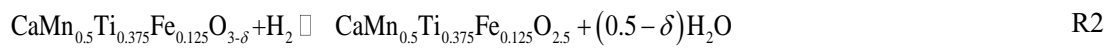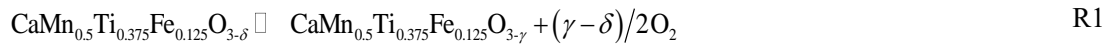
CaMnO$_{3\text{-}\gamma'}$ is the reduction state of the perovskite. When γ' value is low, the perovskite oxide has CLOU properties. Therefore, the $R_{OC,ou}$ depends on the δ' and γ' values. However, further reduction to CaMnO$_2$ occurs in the presence of a reducing gas, e.g. CO, H_2 or CH_4. The parameter γ' also depends on temperature, and γ' value can be calculated by Eq. (8).

$$3\text{-}\gamma' = 2.9793 - 1.3286 \times 10^{-4} T \tag{8}$$

The oxygen uncoupling reaction and reduction reaction in H_2 of the CaMn$_{0.5}$Ti$_{0.375}$Fe$_{0.125}$O$_{3\text{-}\delta}$ perovskite are shown in R2 and R3. Therefore, the oxygen transport capacity for oxygen uncoupling ($R_{OC,ou}$) and the total oxygen transport capacity ($R_{OC,t}$) are calculated as Eqs. (9) and (10). The

calculated $R_{OC,ou}$ and $R_{OC,t}$ for the $CaMn_{0.5}Ti_{0.375}Fe_{0.125}O_{3-\delta}$ perovskite are listed in Table 4. For the

oxygen uncoupling reaction, the O_2 release was not completed during the limited reaction time.

Therefore, the theoretical values of $R_{OC,ou}$ is used to determine the conversion vs time curves for the

oxygen uncoupling kinetics. Fe oxide also acts as oxygen carrier in the $CaMn_{0.5}Ti_{0.375}Fe_{0.125}O_{3-\delta}$

perovskite, which results in the actual values of the total oxygen transport capacity ($R_{OC,t}$) higher

than the values in Table 4. Thus, final values of the total oxygen transport capacity ($R_{OC,t}$) had to be

evaluated by experimental results. For instance, the calculated $R_{OC,t}$ is 5.52 wt.% at 900 °C, which

is lower than 5.71 wt.% obtained by experiments, as seen in sections 4.1 and 4.2 . The experiments

to obtain $R_{OC,t}$ were performed in dry H_2 (10 vol.%) for a longer reduction time. The experiments

might cause a deeper reduction of the OCM compared to wet H_2. Water content is usually existed

in a more real CLC condition. It means that the obtained $R_{OC,t}$ in dry H_2 might be little high. However,

the MFB-TGA is limited to permit steam inlet, all the experiments had to be done in dry reaction

gases.

$$CaMn_{0.5}Ti_{0.375}Fe_{0.125}O_{3-\delta} \rightleftharpoons CaMn_{0.5}Ti_{0.375}Fe_{0.125}O_{3-\gamma} + (\gamma-\delta)/2O_2 \qquad \text{R1}$$

$$CaMn_{0.5}Ti_{0.375}Fe_{0.125}O_{3-\delta} + H_2 \rightleftharpoons CaMn_{0.5}Ti_{0.375}Fe_{0.125}O_{2.5} + (0.5-\delta)H_2O \qquad \text{R2}$$

$$R_{OC,ou} = \frac{(\gamma-\delta)M_O}{M_{Ca} + 0.5M_{Mn} + 0.375M_{Ti} + 0.125M_{Fe} + (3-\delta)M_O} \qquad (9)$$

$$R_{OC,t} = \frac{(0.5-\delta)M_O}{M_{Ca} + 0.5M_{Mn} + 0.375M_{Ti} + 0.125M_{Fe} + (3-\delta)M_O} \qquad (10)$$

Table 4 Oxygen transport capacity values calculated by theoretical method

Temperature (°C)	750	800	850	900	930
$R_{OC,ou}$ (wt.%)	0.91	0.90	0.88	0.82	0.70
$R_{OC,t}$ (wt.%)	5.70	5.67	5.61	5.52	5.45

3.2. Reactor model of oxygen uncoupling reaction in MFB-TGA

The oxygen uncoupling reaction will produce an O_2 concentration profile along the axial direction in the bubbling bed reactor, and driving force (C_{eq,O_2}-C_{e,O_2}) is dependent on the O_2 concentration. Therefore, there is a requirement to build a reactor model to analyze the O_2 concentration profile in the reactor and evaluate its influence on the oxygen uncoupling kinetics. The oxygen uncoupling process of the OCM particles in bubbling bed reactor is illustrated in Fig. 4. The OCM particles were evenly distributed inside the silica particles which are located in the emulsion phase, where the oxygen uncoupling reaction occurred. In the bubbling bed, there was an interphase gas interchange between emulsion phase and bubble phase, and the O_2 released from the OCM particles was transferred from the emulsion phase to the bubble phase, as shown in Fig. 4. For every OCM particle, gaseous O_2 from the chemical reaction was released through external gas diffusion to the emulsion phase. In order to evaluate the influence of the gas phase O_2 concentration and mass transfer between the phases on the kinetics of oxygen uncoupling reaction, a reactor-scale model coupled with the oxygen uncoupling reaction kinetics was built to analyze the experimental data measured by MFB-TGA.

① OCM in the bubbling bed reactor; ② Interphase gas interchange; ③ External gas diffusion; ④ Oxygen uncoupling reaction
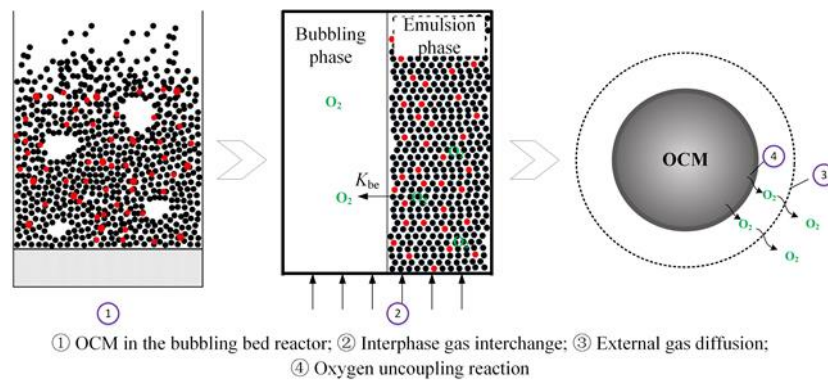
Fig. 4. Oxygen uncoupling reaction process in bubbling bed reactor

The classic K-L model that describes the gas diffusion between the bubble phase and the emulsion phase and chemical reaction in a fluidized bed was applied here [26]. This work assumes that all the OCM particles are only existed in the emulsion phase, and the oxygen uncoupling reaction are first order, as shown in Fig. 4. For the Geldart B particles, the mass transfer occurs directly between the bubble and emulsion phase. Eq. (11) describes the mass balance of released O_2 in the emulsion phase and bubble phase.

$$\begin{cases} -(1-\theta)U_{mf}\dfrac{dC_{e,O_2}}{dz} = -f_a(1-\theta)(1-\varepsilon_{mf})K_r\left(C_{eq,O_2}-C_{e,O_2}\right)+\theta K_{be}(C_{e,O_2}-C_{b,O_2}) \\[4mm] -U_b^*\dfrac{dC_{b,O_2}}{dz} = -K_{be}(C_{e,O_2}-C_{b,O_2}) \end{cases} \tag{11}$$

where C_{b,O_2} (mol/m³) is the O_2 concentration in the bubble phase, C_{e,O_2} (mol/m³) is the O_2 concentration in the emulsion phase, and C_{eq,O_2} (mol/m³) is the O_2 concentration at equilibrium. f_a is the volume fraction of the OCM particles in all solid volume. U_b^* (m/s) is the effective gas velocity in the bubble phase, and U_{mf} (m/s) is the minimum fluidization velocity, as the gas velocity in the emulsion phase. The driving force of the oxygen uncoupling reaction is (C_{eq,O_2}-C_{e,O_2}). The O_2 concentration in the emulsion phase (C_{e,O_2}) has a negative effect on the chemical reaction. All the coefficients and the analytical solution of Eq. (11) are calculated in the below section. K_r is the comprehensive reaction rate constant, with specific expressions:

$$\begin{cases} K_r = \dfrac{1}{\dfrac{1}{K_{ri}}+\dfrac{d_p}{6k_g}} \\[6mm] K_{ri} = \dfrac{R_{OC,ou}\rho_s}{2M_O}\left\{k_{chem}(\psi X_e - X_{chem})^{2/3}+k_{diff}[(1-\psi)X_e - X_{diff}]^{2/3}\right\} \\[4mm] k_g = \left(Sh\cdot D_{O_2}\right)\big/d_p \end{cases} \tag{12}$$

Where K_{ri} (s⁻¹) is the comprehensive reaction rate constant of the particle, k_g (m/s) is the external mass transfer coefficient, and Sh is the Sherwood number .

The kinetic model for the oxygen uncoupling reaction has to take the O_2 concentration at equilibrium into account because the driving force of the reaction is (C_{eq,O_2}-C_{e,O_2}). The kinetic model of oxygen uncoupling is used to calculate the change of the conversion rate, and some kinetic models have been applied for this purpose from literatures, such as the apparent model [18,27], the grain model [28,29], and the rate equation theory [30,31]. A semi-empirical model was applied here to describe the conversion curves of the oxygen uncoupling reaction, as shown in Eq. (13). A faster reaction stage and a slower reaction stage are included, and the total conversion level for the oxygen uncoupling reaction is equal to the sum of conversion levels for the first stage and the second stage.

$$\begin{cases} \dfrac{dX_{chem}}{dt} = k_{chem}(\psi X_e - X_{chem})^{2/3}\left(C_{eq,O_2}\text{-}C_{e,O_2}\right) \\ \dfrac{dX_{diff}}{dt} = k_{diff}[(1-\psi)X_e - X_{diff}]^{2/3}\left(C_{eq,O_2}\text{-}C_{e,O_2}\right) \\ X = X_{chem} + X_{diff} \end{cases} \qquad (13)$$

where k_{chem} (m³/mol/s) and k_{diff} (m³/mol/s) are the reaction rate constants of the different reaction stages, ψ is the ratio of the conversion level at the fast stage to the equilibrium conversion level, and the value of ψ depends on the reaction temperature, which can be expressed as Arrhenius equation. 2/3 is a semiempirical exponential factor. X_{chem} and X_{diff} correspond to the conversion levels during the fast reaction stage and the slow reaction stage, respectively.

3.3. Reactor model of oxidation and reduction reactions in MFB-TGA

For the oxidization and reduction reactions, reaction gases, from the fluidizing agents, are diffused from the bubble phase to the emulsion phase, further transferred to the surface of the OCM particles. Taken the reduction with H_2 as example, the OCM particles are distributed in the emulsion phase, and the reaction gas, H_2, is existed in the bubble phase, initially. Next, the reduction process in bubbling bed rector contains the following steps: gas interchange from bubble to emulsion phases

in the bubbling bed; external gas diffusion to the particle surface; chemical reaction, as seen in Fig. 5. The process is different from the oxygen uncoupling reaction.
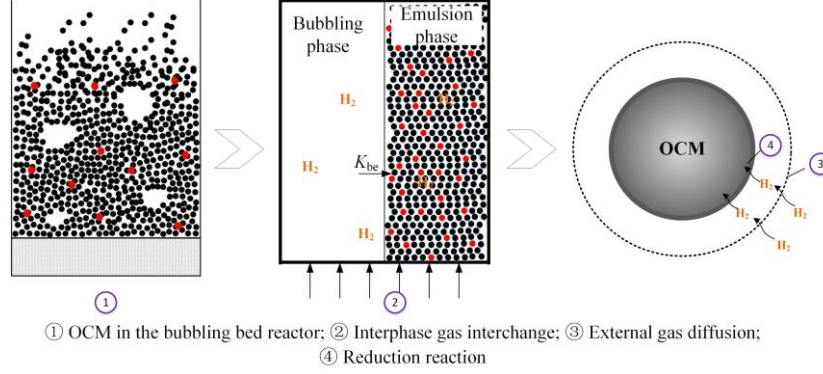

① OCM in the bubbling bed reactor; ② Interphase gas interchange; ③ External gas diffusion;
④ Reduction reaction

Fig. 5. Reduction reaction process with H_2 in bubbling bed reactor

To analyze the MFB-TGA experimental data, the classic fluidization bed reactor model developed by Kunii and Levenspiel (K-L model) was also used to describe the reaction behavior and the mass transfer between the bubble and emulsion phase [26]. Considering the mass balance in the bubble and emulsion phase, the K-L model can be expressed as:

$$\begin{cases} -U_b^* \dfrac{dC_{b,i}}{dz} = K_{be}(C_{b,i} - C_{e,i}), (i = O_2, H_2, CH_4) \\ -(1-\theta)U_{mf}\dfrac{dC_{e,i}}{dz} = -\theta K_{be}(C_{b,i} - C_{e,i}) + f_a(1-\theta)(1-\varepsilon_{mf})K_r\left(C_{e,i} - C_{eq,i}\right), (i = O_2, H_2, CH_4) \end{cases} \quad (14)$$

where K_r (s^{-1}) is the comprehensive reaction rate constant, including the gas-solid reactions and the impact of the external mass transfer resistance. In this work, the rate constant K_r is expressed by Eq. (15). k_g (m/s) is the external mass transfer coefficient. D_i (m^2/s) is the molecular diffusivity of gas i in N_2.

$$\begin{cases} K_r = \dfrac{1}{\dfrac{1}{K_{ri}} + \dfrac{d_p}{6k_g}} \\ K_{ri} = \dfrac{R_{o,t}\rho_s}{\alpha M_O}\left\{k_{chem}(\psi X_e - X_{chem})^{2/3} + k_{diff}[(1-\psi)X_e - X_{diff}]^{2/3}\right\} \\ k_g = \left(Sh \cdot D_i\right)/d_p, \quad (i = O_2, H_2, CH_4) \end{cases} \quad (15)$$

The gas-solid reaction usually includes two stages, i.e., a faster stage dominated by the chemical reaction and a slower stage controlled by mass transfer through the product layer around the non-porous spherical grains. The semiempirical model containing the two stages was also applied to describe the conversion curves of the oxidation and reduction reactions, c.f. Eq. (16). The conversion levels of the first stage (X_{chem}) and the second stage (X_{diff}) are described by the classic grain model, and the second stage starts from the end of the fast stage (critical conversion, ψX_e). Finally, the total conversion level of a reaction is the sum of the two stages. k_{chem} and k_{diff} ($m^3/mol/s$) represent the reaction rate constants of the fast reaction stage controlled by chemical reaction mechanism and the second reaction stage controlled by diffusion through the product layer mechanism, respectively. The exponent of the two stages, 2/3, is a known parameter in the model.

$$
\begin{cases}
\dfrac{dX_{chem}}{dt} = k_{chem}(\psi X_e - X_{chem})^{2/3}\left(C_{e,i} - C_{eq,i}\right), \quad (i = O_2, H_2, CH_4) \\[2mm]
\dfrac{dX_{diff}}{dt} = k_{diff}[(1-\psi)X_e - X_{diff}]^{2/3}\left(C_{e,i} - C_{eq,i}\right), \quad (i = O_2, H_2, CH_4) \\[2mm]
X = X_{chem} + X_{diff}
\end{cases}
\tag{16}
$$

The impact factor of the external mass transfer, defined as the ratio of the external mass transfer rate to the consumption rate, is shown in Eq. (17). The ratio of the consumption rate in the emulsion phase to the mass transfer rate between the bubble phase and the emulsion phase is shown in Eq. (18), in order to evaluate the influence of the mass transfer between phases.

$$
I_1 = \frac{\pi d_p^2 k_g}{R_{o,t} \rho_s \dfrac{\pi d_p^3}{6\alpha M_o}(k_{chem}(\psi X_e - X_{chem})^n + k_{diff}((1-\psi)X_e - X_{diff})^n)}
\tag{17}
$$

$$
I_2 = \frac{f_a K_r(1-\theta)(1-\varepsilon_{mf})}{\theta K_{be}}
\tag{18}
$$

3.4. Model parameter calculation

Here, a detailed calculation of the parameters related to the reactor models for the oxygen uncoupling and redox reactions is included.

The minimum fluidization velocity was calculated by the Ergun equation [32]:

$$U_{mf} = \frac{\left[33.7^2 + 0.0408 d_p^3 \rho_g (\rho_s - \rho_g) g / \mu^2\right]^{0.5} - 33.7}{d_p \rho_g / \mu} \tag{19}$$

The effective gas velocity in the bubble phase, U_b^* (m/s), was calculated based on the gas balance in cross section of the fluidized bed:

$$U_b^* = \frac{U_0 - (1-\theta)U_{mf}}{\theta} \tag{20}$$

Where U_0 (m/s) is the superficial gas velocity. The bubble fraction, θ, can be estimated by the expression put forward by Abanades et al. [33]:

$$\theta = \frac{U_0 - U_{mf}}{U_b + \dfrac{5U_{mf} - \varepsilon_{mf}U_b}{4}} \quad \text{for} \quad 1 < \frac{\varepsilon_{mf}U_b}{U_{mf}} < 5 \tag{21}$$

ε_{mf} is the bed voidage at minimum fluidization state. The bubble rise velocity can be obtained as:

$$U_b = U_0 - U_{mf} + 0.711(g \cdot d_b)^{1/2} \tag{22}$$

The bubble diameter, d_b (m), is calculated as a function of the bed height z:

$$d_b = 0.54(U_0 - U_{mf})^{0.4} z^{0.8} / g^{0.2} \tag{23}$$

In Eqs. (11) and (14), K_{be} (s^{-1}) is the overall gas interchange coefficient between bubble and emulsion phases, and can be calculated as:

$$K_{be} = 4.5 \frac{U_{mf}}{d_b} \tag{24}$$

In addition, the relationship between the bed height and the bubble phase fraction is expressed as:

$$\theta = \frac{H - H_{mf}}{H_{mf}} \tag{25}$$

In the reactor models, the Sherwood number in the calculation of the value of k_g is determined according to Chuang et al. [18]:

$$Sh = 2\varepsilon_{mf} + 0.69(R_e / \varepsilon_{mf})^{1/2} Sc^{1/3} \tag{26}$$

Where R_e is the Reynolds number, and Sc is the Schmidt number.

3.5. Calculation algorithm

The analytical solution for Eq.s (11) and (14) can yield the gas axial concentration profile in the fluidized bed. The boundary condition is as follows: when z=0, $C_{b,i}=C_{e,i}=C_{i,0}$. For the oxygen uncoupling in pure N_2, $C_{O_2,0}$ is thought to be 10^{-6} mol/m^3. Then the concentration of gas i in emulsion phase at height z can be solved:

$$C_{e,i,z}=C_{eq,i} + \left(C_{i,0} - C_{eq,i}\right)\frac{\theta}{(1-\theta)\Phi}\left[(1-\psi_2)\exp(-q_1 z) + (\psi_1 - 1)\exp(-q_2 z)\right], (i = O_2, H_2) \tag{27}$$

The concentration of gas i in emulsion phase was then calculated by:

$$C_{b,i,z}=C_{eq,i} + \left(C_{i,0} - C_{eq,i}\right)\frac{\theta}{(1-\theta)\Phi}\left[\frac{(1-\psi_2)(1-\exp(-q_1 z))}{q_1 z} + \frac{(1-\psi_1)(1-\exp(-q_2 z))}{q_2 z}\right], (i = O_2, H_2, CH_4) \tag{28}$$

The parameters used in Eqs. (27)-(28) are calculated as:

$$q_1 = \frac{1}{2}\frac{f_a K_r}{U_{mf}}(1-\varepsilon_{mf}) + \frac{1}{2}\frac{K_{be}}{U_{mf}}\left(\frac{\theta}{1-\theta} + \frac{U_{mf}}{U_b^*} - \Phi\right) \tag{29}$$

$$q_2 = \frac{1}{2}\frac{f_a K_r}{U_{mf}}(1-\varepsilon_{mf}) + \frac{1}{2}\frac{K_{be}}{U_{mf}}\left(\frac{\theta}{1-\theta} + \frac{U_{mf}}{U_b^*} + \Phi\right) \tag{30}$$

$$\psi_1 = \frac{1}{2} - \frac{1-\theta}{2\theta}\left[\frac{U_{mf}}{U_b^*} - \frac{f_a K_r}{K_{be}}(1-\varepsilon_{mf}) - \Phi\right] \tag{31}$$

$$\psi_2 = \frac{1}{2} - \frac{1-\theta}{2\theta}\left[\frac{U_{mf}}{U_b^*} - \frac{f_a K_r}{K_{be}}(1-\varepsilon_{mf}) + \Phi\right] \tag{32}$$

$$\Phi = \left[(\frac{f_a K_r}{K_{be}}(1-\varepsilon_{mf}))^2 + (\frac{\theta}{1-\theta} + \frac{U_{mf}}{U_b^*})^2 + 2(\frac{f_a K_r}{K_{be}}(1-\varepsilon_{mf}))(\frac{\theta}{1-\theta} + \frac{U_{mf}}{U_b^*})\right]^{1/2} \tag{33}$$

Whether it is the oxygen uncoupling reaction or redox reaction, the axial distribution of the gas concentration is variable in the emulsion phase. In this work, the average gas concentration in the

emulsion phase calculated by Eq. (34) was applied to calculate the conversion levels in Eqs. (13) and (16).

$$C_{e,i,ave} = z^{-1} \int_0^z C_{e,i} dz, \ (i = O_2, H_2, CH_4) \tag{34}$$

In the reactor models, it is assumed that every solid reactant particle has the same reaction behavior, and the gas concentration around every particle is equal to the average gas concentration in the emulsion phase. The conversion levels for the oxygen uncoupling and redox reactions were calculated by Eqs. (13) and (16). The flowchart of the calculation algorithm is shown in Fig. 6. The conversion versus time curves can be obtained as the solving steps. Finally, the activation energies can be obtained based on the rate constants (k_{chem}, k_{diff}) at different temperatures.
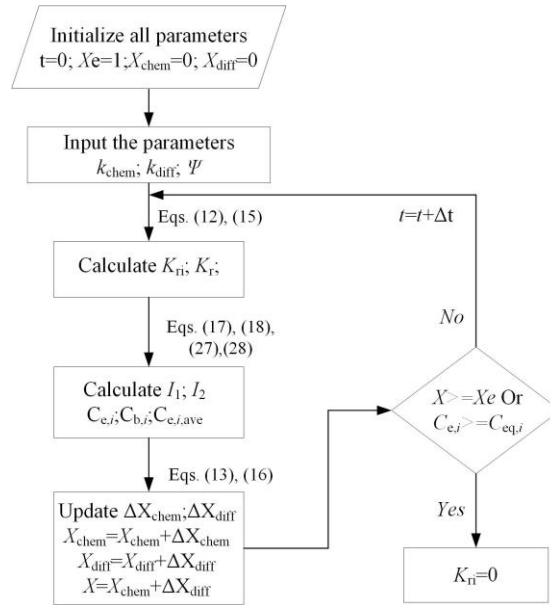
Fig. 6. Flowchart of the calculation algorithm

4. Results

4.1. Multicycles of oxygen carrier in MFB-TGA

Fig. 7 shows the redox multicycles of oxygen carrier at 900 °C and how the OCM behaves under different oxidization and reduction times. The first cycle had the longest reduction time to obtain the total oxygen transport capacity ($R_{OC,t}$). A mass loss of 5.71 wt.% means that the value of

$R_{OC,t}$ is equal to 5.71 wt.%. After that, a series of 3 cycles was performed for a reduction/oxidization period of 120/60 s, achieving a stable total oxygen transport capacity of 5.71 wt% as well. Interestingly, when further shortening the reduction/oxidation period to 60/30 s, the stable total oxygen transport capacity of 5.71 wt% was still kept for another 20 redox cycles. The multicycle results indicate that the OCM can transfer the lattice oxygen effectively and quickly. The OCM can stay stable under redox reactions with different durations of the reduction/oxidization period, and its reactivity has no decay with number of cycles. It can be concluded that the synthetic perovskite oxide is very stable and high reactivity. The rate of oxidization reaction is very fast because the needed time for the OCM regeneration is less than 30 s.
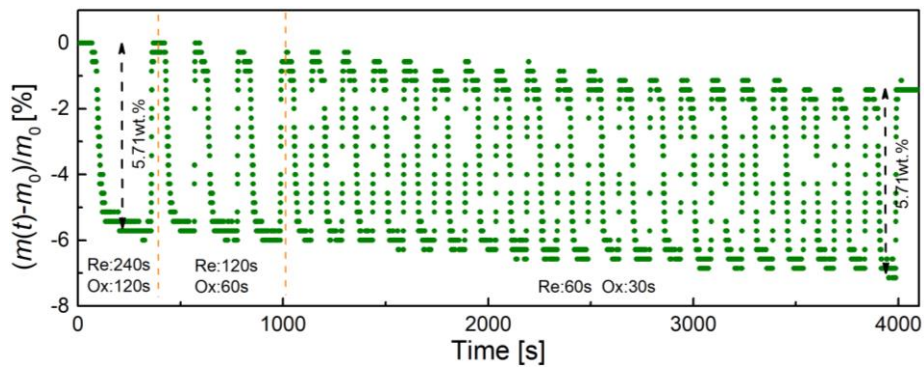
Fig. 7. Multicycles of mass variation during redox cycles in the MFB-TGA at 900ºC (Oxidization: 21 vol.% O_2, Reduction: 10 vol.% H_2)

4.2. Typical results obtained by the MFB-TGA experiments

For each test, the original experimental data consisted of a series of real-time mass signals and pressure difference signals. The mass signals recorded in the MFB-TGA were used to calculate the mass variation caused by the oxygen uncoupling or gas-solid reactions. Taking the test at 900 ºC as an example, mass variation and differential pressure signals for the oxygen uncoupling and the redox reactions are shown in Figs. 8(a) and (b). For the oxygen uncoupling reaction, the mass loss was approximately 16 mg, corresponding a mass change of 0.53 wt.%. The mass loss was lower than

0.82 wt.% acquired by theoretical calculation. It indicated that the oxygen uncoupling cannot be completed within 300 s, since the second reaction stage was quite slow. According to Leonidova et al. [8], the rate of the oxygen uncoupling reaction became slow with increasing time because the driving force (C_{eq,O_2}-C_{e,O_2}) decayed significantly. As a result of decrease in the values of (3-δ), the equilibrium O_2 concentration ($C_{O_2,eq}$) would be extremely low according to Eq. (5). During the oxidation stage, the OCM particles could be completely re-oxidized at a fast reaction rate. For the redox reaction in Fig. 8(b), the amount of mass loss was ~ 20 mg, corresponding to an oxygen transport capacity of 5.71 wt.%. It can be seen from the figure that it takes ~ 30 s to complete the reduction reaction. Then the mass variation was stable at ~ 5.71 wt.%. The reduction rate in 10% vol.% H2 was relatively fast compared with the oxygen uncoupling rate, as expected from the higher driving force. The mass increase happened in a very short time for the oxidation reaction, similar as the re-oxidization of the OCM particles after oxygen uncoupling. From Figs. 8(a) and (b), the stable fluctuation of the differential pressure curves implied that the good fluidization was kept and the fluidization performance of the OCM particles was satisfied, which shows a good mass and heat transfer during the oxygen uncoupling and redox reactions.
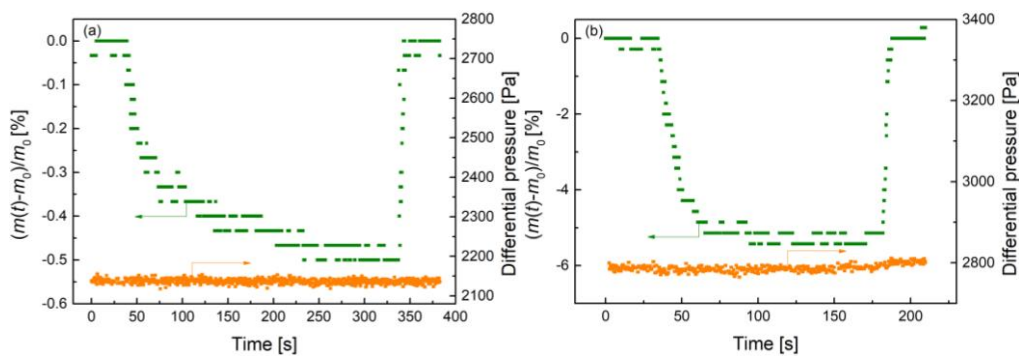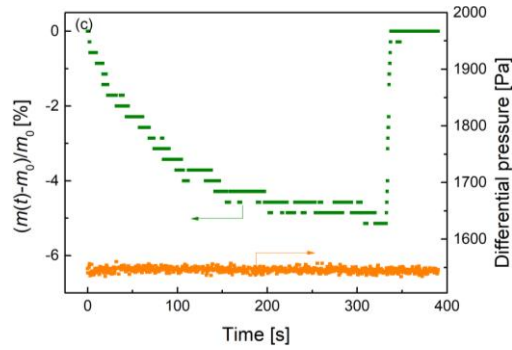
Fig. 8. Mass variation and differential pressure signals during (a) oxygen uncoupling reaction at

900 °C, (b) redox reaction with 21 vol.% O_2/ 10vol.% H_2 at 900 °C and (c) redox reaction with 21

vol.% O_2/10vol.% CH_4 at 900 °C

In addition, Fig. 9(a) compares the oxygen uncoupling kinetics conducted by the MFB-TGA

and a regular TGA (Q500) at 900 °C. The first stage has a big difference between the two results,

and the reaction rate of obtained by the MFB-TGA is much faster than that obtained by Q500. In

Q500, the released O_2 is relatively difficult to diffuse to the main gas stream in time due to poor

mass transfer. The O_2 concentration around the particles in TGA are higher than that in the MFB-

TGA, which causes that the driving force of the oxygen uncoupling is very low. Hence, a limited

reaction rate in Q500 occurred. The comparison proves that the MFB-TGA with the capability of

fast mass transfer is a useful tool to obtain a more accurate kinetic result under fluidization states
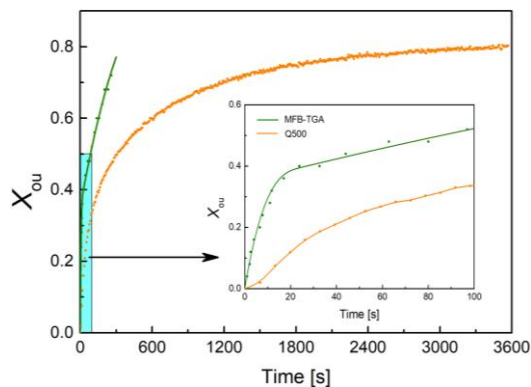
[21,23].

Fig. 9. Comparison of the oxygen uncoupling kinetics conducted by the MFB-TGA and a regular

TGA (Q500) at 900°C

4.3. Kinetics determination for oxygen uncoupling reaction

The kinetics of oxygen uncoupling reaction was determined at 800-930 °C, and the tested OCM

particles were treated by 10 vol.% H_2 for 6 cycles, considering the actual experience in the fuel

reaction. Fig. 10 shows the experimental and model results of the oxygen uncoupling reaction. The

conversion vs time curves are composed of a fast reaction stage and a slow reaction stage. Overall,

the rate of oxygen uncoupling is decreased with time, and the reason has been discussed in section

4.2. Temperature has an influence on the reaction rate, which is enhanced by the rising temperature.

For example, it takes ~ 18 s to acquire a conversion level of 0.4 at 930 °C, but it requires ~ 40 s at

900 °C and >100 s at 800-850 °C for the same conversion level. Above model was applied to fit the

experimental data. To obtain the range of k_{chem} and k_{diff}, 3 repeated experimental results were used

to determine the error range. Fig. 10(a), as a representative, the values of k_{chem} and k_{diff} are at the

range of 0.0039-0.0041 $m^3mol^{-1}s^{-1}$ and 0.00011-0.00013 $m^3mol^{-1}s^{-1}$ at 900 °C, respectively. Hence,

the parameters, k_{chem} and k_{diff}, are the average values of themselves. Finally, all the values of k_{chem}

and k_{diff} are determined at the tested temperatures, as shown in Fig. 10(b). The model can well

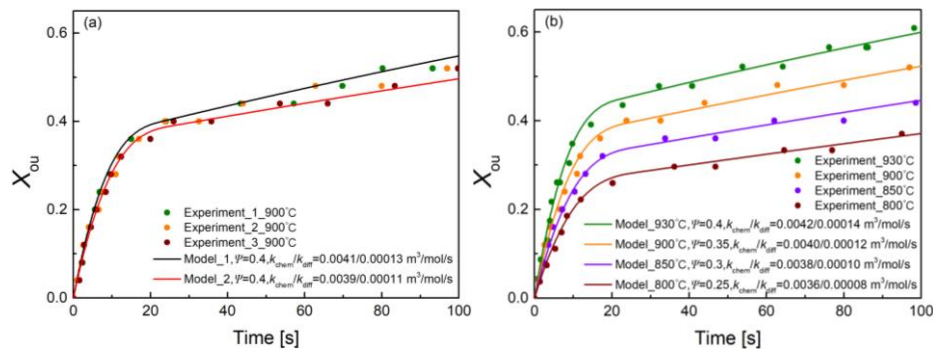reproduce the experimental data at various temperatures.

Fig. 10. Kinetics of the oxygen uncoupling reaction (a) obtainment of the rate constant of at

900 °C and (b) conversion vs time curves at different temperatures

According to the above model, the gaseous O_2 concentrations in the emulsion and bubble phases were calculation. The axial profiles of O_2 concentrations in the emulsion and bubble phases at the beginning of the oxygen uncoupling reaction at 930 ºC are plotted in Fig. S1. Under the present experimental conditions, the O_2 concentrations across the whole bed are ~ 0.1 vol. %, which is far lower than the equilibrium O_2 concentration ($C_{O_2,eq}$) calculated by Eq. (5), which ensures that the effect of O_2 concentration can be neglected and the driving force of the oxygen uncoupling reaction (C_{eq,O_2}-C_{e,O_2}) is always positive.

Fig. 11 shows the Arrhenius plots of $\ln(\Psi)$, $\ln(k_{chem})$ and $\ln(k_{diff})$ of the oxygen uncoupling reaction as the function of $1/T$. The kinetic parameters are listed in Table 5. The slope of $\ln(\Psi)$, $\ln(k_{chem})$ and $\ln(k_{diff})$ vs $1/T$ curves determines the values of ($-E_L/R_g$), ($-E_{chem}/R_g$) and ($-E_{diff}/R_g$), from which the activation energies, E_L, E_{chem} and E_{diff} were calculated. The pre-exponential factors for the first and second stages ($-A_{0,L}$, $-A_{0,chem}$ and $-A_{0,diff}$) were determined from the intercepts of the plots.
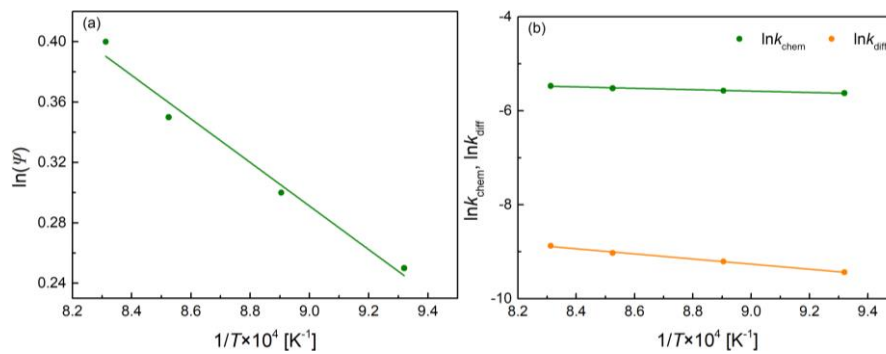

Fig. 11. Arrhenius plots to calculate the kinetic parameters for the oxygen uncoupling reaction (a) $\ln(\Psi)$ vs $1/T$ and (b) $\ln(k_{chem})$ and $\ln(k_{diff})$ vs $1/T$

Table 5 Summary of kinetic parameters for the oxygen uncoupling reaction

Parameter	E_L	E_{chem}	E_{diff}	$A_{0,L}$	$A_{0,chem}$	$A_{0,diff}$
Unit	kJ/mol	kJ/mol	kJ/mol	n.a.	m³/mol/s	m³/mol/s
Value	37.86	12.36	45.12	17.33	1.43×10^{-2}	1.25×10^{-2}

4.4. Kinetics determination for oxidization and reduction reactions

The oxidization kinetics in the range of 700 to 900 °C were carried out to evaluate the effect of

temperature. Fig. 12 illustrates experimental and model results of the conversion vs time curves for

the OCM particles. The required time for full regeneration in 21vol.% O_2 is only ~ 5 s in the

temperature range. It means that the kinetics of the oxidization reaction is insensitive to the

temperature. Even for the oxidization at 700 °C, the reaction rate is still fast. The weak effect of

temperature on the oxidization of perovskite oxides was also found by the researchers from ICB-

CSIC, Spain [10] . The rising temperature of the OCM particle during the exothermic oxidization

reaction was calculated by using a steady-state heat balance, see the supplementary material. The

particles temperature just increased by 10-21 °C at d_p=200 μm, due to the fast heat transfer in a

fluidization bed. In the MFB-TGA, the majority of bed materials is silica sand, and only 350 mg of

OCM particles are dispersed in the emulsion phase. The produced heat can be quickly transferred

by convection and radiation. Even for the ultrafast reaction, an approximately isothermal reaction

conditions could be created in the MFB-TGA [21]. An interesting finding is that the oxidization step

only consists of the first fast reaction stage, which is very different from the other gas-solid reaction

kinetics, such the oxidization of manganese ore [21], ilmenite [34] and Tierga iron ore [35]. This

behavior shows that the mechanism of the oxidization reaction was just controlled by the chemical

reaction during the whole oxidization process. The kinetic model was applied to simulate the

experimental results. Fig. 12(a) shows how to determine the range of k_{chem}, and the parameter k_{chem} is 0.54-0.58 m³mol⁻¹s⁻¹ at 900 °C. The model results at different temperatures are illustrated in Fig. 12(b). It should be noted that the parameter Ψ is set to 1, considering that only the first reaction stage occurred for the oxidization processes.
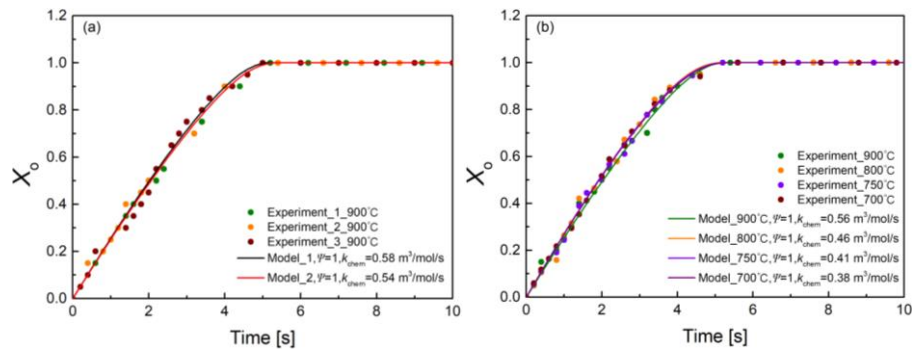

Fig. 12. Kinetics of the oxidization reaction (a) obtainment of the rate constant of at 900 °C and

(b) conversion vs time curves at different temperatures

If the consumption rate of O_2 is close to the rate of mass transfer, the reaction kinetics is impossible to determine. Thus, the O_2 concentration inside the emulsion phase should be followed. The results are shown in Fig. S2. The O_2 concentrations at the MFB outlet are increased from 1.98 vol.% to 21 vol.% for oxidization at 900 °C. The O_2 in emulsion phase was not completely depleted at the beginning of the oxidization reaction. The consumption rate of O_2 is slower than the rates of external diffusion and mass transfer between the two phases. Thus, the obtained kinetics controlled by the chemical reaction mechanism are reliable.

Parts (a) and (b) of Fig. 13 show the conversion vs time curves of the reduction reaction in 10 vol.% H_2 in the range of 700-900 °C. According to the experimental results, the reduction kinetics can be divided into the fast initial stage and the slow second stage, which is caused by a change in the controlling mechanism during the gas-solid reaction. The reduction is mainly controlled by the chemical reaction at low conversion levels, but the gas diffusion through the formed product layer

controls the reaction at high conversion levels. The rate of reduction reaction increased as the temperature rose from 700 °C to 900 °C, and the effect was more significant for the second reaction stage. Fig. 13(a) illustrates the values of k_{chem} and k_{diff} are 0.22 ± 0.02 m³mol⁻¹s⁻¹ and 0.04 ± 0.02 m³mol⁻¹s⁻¹ at 900 °C. The model results in the range of 700-900 °C are shown in Fig. 13(b). The two-stage model could agree the experimental results well.
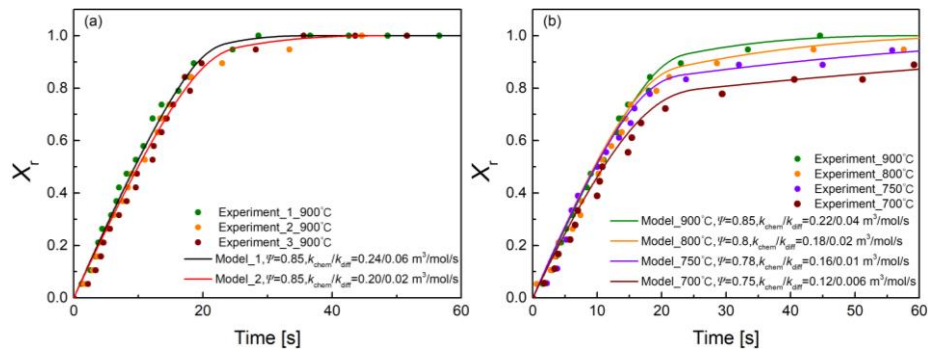

Fig. 13. Kinetics of the reduction reaction with H_2 (a) obtained rate constant at 900 °C and

(b) conversion vs time curves at different temperatures

Fig. S3(a) presents the average H_2 concentration in the emulsion and the ratio I_2 during the reduction process at 900 °C. The mass transfer rate between the bubble and emulsion phases is faster than the rate of H_2 consumption. The effect of the external mass transfer was also evaluated, see Fig. S3(b). The value of K_{ri} was significantly less than that of $(6k_g/d_p)$, indicating that the effect of the external gas diffusion can be neglected. The axial distribution of H_2 in the emulsion and bubble phases at the beginning of the reduction reaction is shown in Fig. S3(c). The H_2 in emulsion phase was not completely depleted at the beginning of the oxidization reaction.

The conversion vs time curves of the reduction reaction in 10 vol.% CH_4 at 800-900 °C are illustrated in Figs. 14(a) and (b). As same as reduction by H_2, the conversion vs time curves of reduction reaction with CH_4 are composed of an initial fast reaction stage controlled by chemical reaction mechanism and a second slow reaction stage controlled by gas diffusion mechanism

through product layer as well. The reduction rates are quite slow compared with above reduction by H_2 and oxidization, even for the reaction at 900 °C. With the increase in temperature, a conversion rate can be enhanced. Taking the reaction at 900 °C for an example, the rate constants, k_{chem} and k_{diff}, are 0.012 ± 0.002 m^{3}mol^{-1}s^{-1} and 0.0008 ± 0.0002 m^{3}mol^{-1}s^{-1} acquired by repeatable experiments, c.f. Fig. 14(a). The fluidized bed model with a kinetic model could describe the two-stage reaction property very well, c.f. Fig. 14(b).
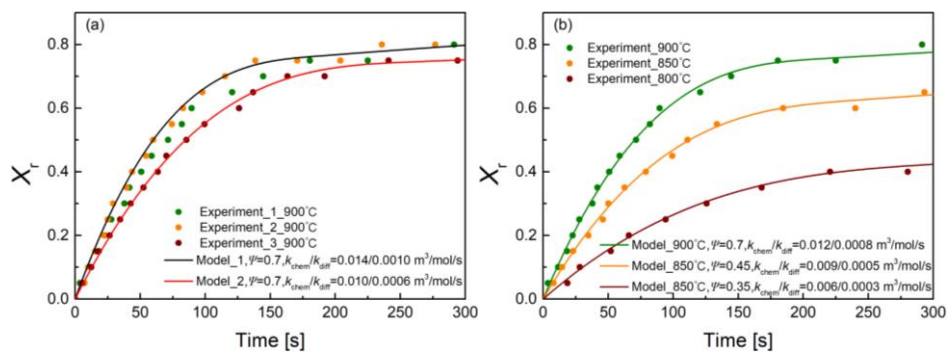

Fig. 14. Kinetics of the reduction reaction with CH_4 (a) obtainment of the rate constant of at 900 °C and (b) conversion vs time curves at different temperatures

Also, the average CH_4 concentration in the emulsion phase and the impact of interphase gas exchange, I_2, were estimated during the reduction process at 900 °C, as seen in Fig. S4(a). The impact of external mass transfer, I_1, was also evaluated in Fig. S4(b). The mass transfer rate is faster than the CH_4 consumption rate in the emulsion phase. The effect of the external mass transfer can be neglected. The axial distribution of CH_4 in the emulsion and bubble phases at the beginning of the reduction by CH_4 is shown in Fig. S3(c).

Based on above model results of the oxidization and reduction reactions, the Arrhenius plots of $\ln(\Psi)$, $\ln(k_{chem})$ and $\ln(k_{diff})$ of the oxidization and reduction reactions a function of $1/T$ can be obtained, as shown in Fig. 15. The activation energies for the critical conversion level, chemical reaction control and the diffusion in the product layer, E_L, E_{chem} and E_{diff}, were calculated from the

slope of the plots, while pre-exponential factors, $A_{0,\text{L}}$, $A_{0,\text{chem}}$ and $A_{0,\text{diff}}$, were calculated from the intercept. Table 6 is a summary of kinetic parameters for the oxidization and reduction reactions.

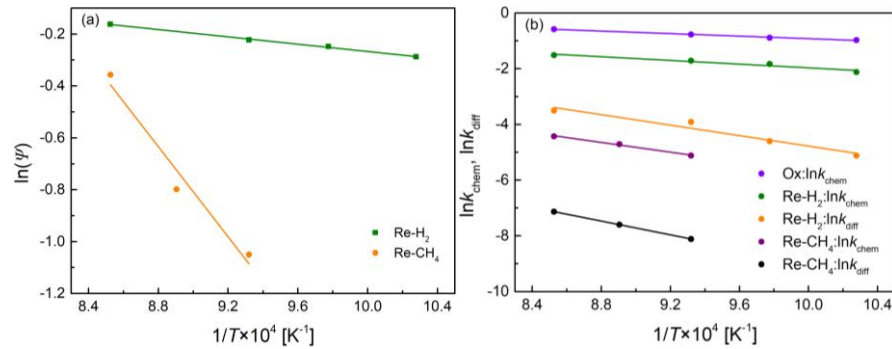

Fig. 15. Arrhenius plots to calculate the kinetic parameters for the oxidization and reduction reactions (a) $\ln(\Psi)$ vs $1/T$ and (b) $\ln(k_{\text{chem}})$ and $\ln(k_{\text{diff}})$ vs $1/T$

Table 6 Summary of kinetic parameters for the oxidization and reduction reactions

Parameter	E_{L}	E_{chem}	E_{diff}	$A_{0,\text{chem}}$	$A_{0,\text{chem}}$	$A_{0,\text{diff}}$
Unit	kJ/mol	kJ/mol	kJ/mol	n.a.	m³/mol/s	m³/mol/s
O_2	n.a.	18.77	n.a	n.a.	3.80	n.a
H_2	5.86	27.62	78.13	1.55	3.86	1.01×10^2
CH_4	72.19	72.67	102.63	1.10×10^2	20.98	29.74

4.5. Characterization of morphology

Fig. 16 shows the surface morphology of the fresh and tested $CaMn_{0.5}Ti_{0.375}Fe_{0.125}O_{3-\delta}$ particles. The fresh particles, prepared by the spray drying granulation, are very integral, and these particles are composed of plenty of grains. The grain size is between 2-10 μm, and the grain boundaries are apparently visible at a high magnification. For one grain, there is a very dense and smooth surface. However, apparent cracks on the particles are found for the tested $CaMn_{0.5}Ti_{0.375}Fe_{0.125}O_{3-\delta}$. Although the grain boundaries are still clear, the surface of one grain becomes rough. These texture presenting on the grain surface will contribute to an increase in surface area, which is beneficial to the chemical reaction in term of gas-solid contact. Since the experiments were done in the dry H_2,

it might reduce the OCM deeply (Ti^{4+} to Ti^{3+} and Fe^{2+} to Fe to some extent).

(a) Fresh OCM

(b) Tested OCM
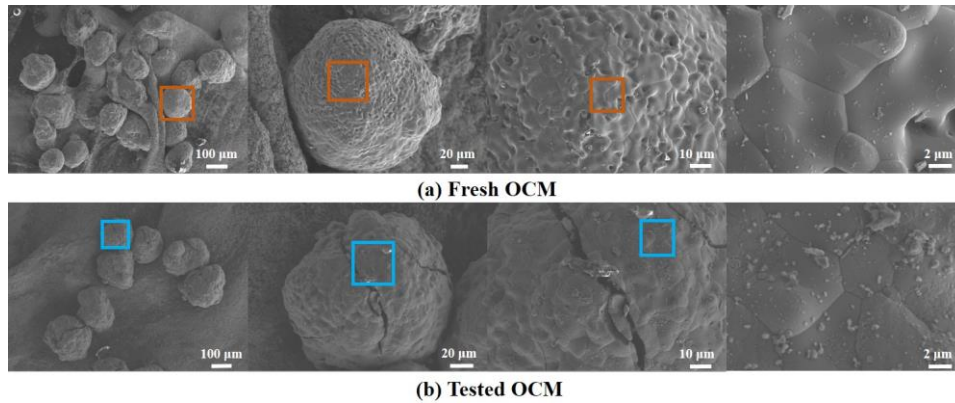
Fig. 16. SEM images of fresh and tested particles

The cross-sectional characterizations of the fresh and tested $CaMn_{0.5}Ti_{0.375}Fe_{0.125}O_{3-\delta}$ particles are illustrated in Fig. 17, and the morphology inner the particles can be observed. The fresh particles are very integral, and many macropores with micron scale distribute inner the particle. Around the macropores, the structure is quite dense. As for the tested particles, inhomogeneity, and cracks are formed inner almost all the particles. These cracks cross the whole particle are possible to bring an attenuation in physical structure, resulting in the particle to be prone to attrition. Not only do the macropores with micron scale distribute inner the particle like the fresh one, but also many micropores are formed and distributed in the cross-sectional area, homogeneously. The newly developed porosity in the form of micropores could help gas diffusion inner the particles, and also increase the space for product layer growth. In this regard, the $CaMn_{0.5}Ti_{0.375}Fe_{0.125}O_{3-\delta}$ can obtain a fast gas-solid reaction kinetics, especially for the oxidization reaction. From Fig. 18, the constituting elements are homogeneously distributed within one grain, and no element migration or enrichment occurred during the test, which indicates that the chemical structure of the perovskite oxide is stable under such a harsh redox condition.
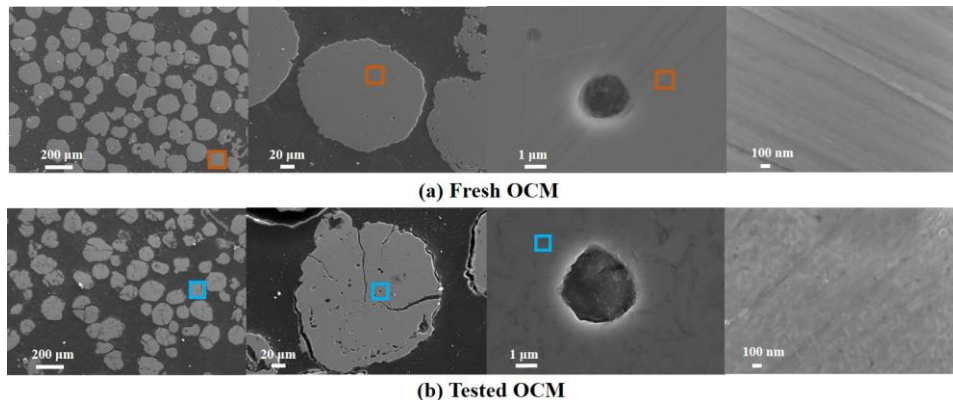

(a) Fresh OCM

(b) Tested OCM

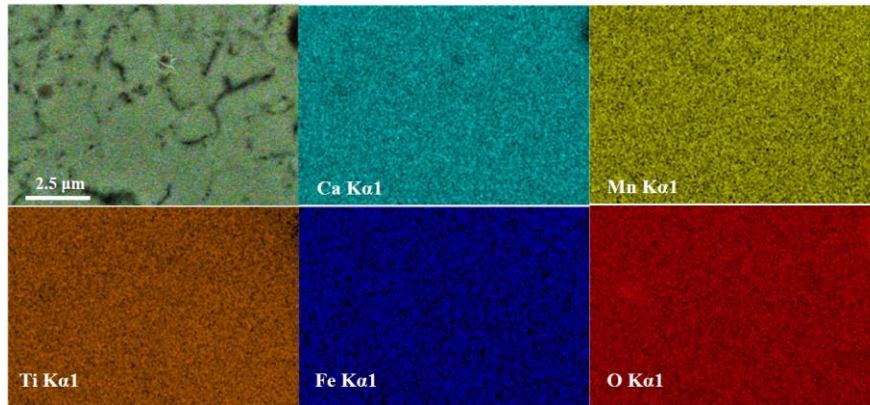Fig. 17. Cross sectional SEM images of fresh and tested particles

Fig. 18. Constituting elements distribution within a grain of the tested particles

5. Discussion

In a CLC unit, the OCM particles circulates between the air reactor and the fuel reactor. Heterogeneous reaction kinetics of an OCM are closely related to reactor design, process demonstration and optimization. For instance, the oxygen uncoupling and reduction kinetics affect the fuel conversion by CLOU and CLC modes in the fuel reactor [36]. The oxidation reaction of an OCM is a highly exothermic reaction, which causes the oxidation kinetics play an important role on the heat manage inside the air reactor, to avoid a hot pot problem. According to Abad et al. [36], the required minimum bed inventories (kg/MW) in the fuel reactor and air reactor are mainly dominated by the heterogeneous reaction rate (dX/dt). Developing an OCM with fast heterogeneous reaction kinetics can reduce the requirement for the bed inventories, which is economy effectively in terms of the development of the CLC technology. In this work, the heterogeneous reaction rates of $CaMn_{0.5}Ti_{0.375}Fe_{0.125}O_{3-\delta}$ are compared with the mainstream OCMs.

In Fig. 19, the oxygen uncoupling rates of the selected OCMs were compared at the same condition (900 °C, pure N_2). The results of $CaMn_{0.5}Ti_{0.375}Fe_{0.125}O_{3-\delta}$ are calculated by above models, and the results of other OCMs were obtained by TGA method. It can be seen that the oxygen uncoupling kinetics of $CaMn_{0.5}Ti_{0.375}Fe_{0.125}O_{3-\delta}$ measured by MFB-TGA in this work are much faster than that of other OCMs measured by the TGA method, which might be caused by the precise determination of the oxygen uncoupling kinetics due to fast mass and heat transfer in the MFB-TGA.
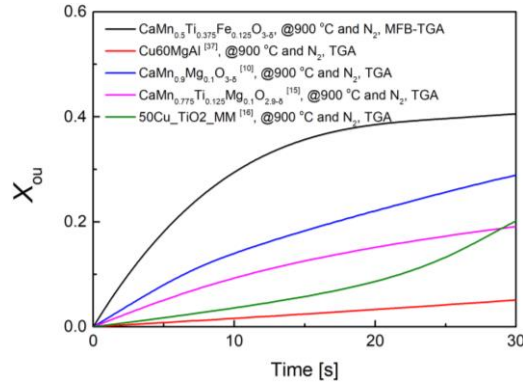
Fig. 19. Comparison of the oxygen uncoupling kinetics for different OCMs

Fig. 20 compares the oxidization and reduction kinetics of $CaMn_{0.5}Ti_{0.375}Fe_{0.125}O_{3-\delta}$ with different OCMs. The oxidization rates were obtained at the same temperature and O_2 concentration, and the reduction rates were obtained at the same temperature but different H_2 concentration (10 vol.% H_2 in MFB-TGA and 15 vol.% H_2 in TGA). In the situation, the kinetics of the reported OCMs universally takes >20 seconds for full oxidation and >60 seconds for full reduction. The newly developed OCM, $CaMn_{0.5}Ti_{0.375}Fe_{0.125}O_{3-\delta}$, has relatively faster oxidization and reduction rates, especially at the initially fast reaction stages. The comparison shows that $CaMn_{0.5}Ti_{0.375}Fe_{0.125}O_{3-\delta}$ is a very promising OCM from the chemical property point of view.
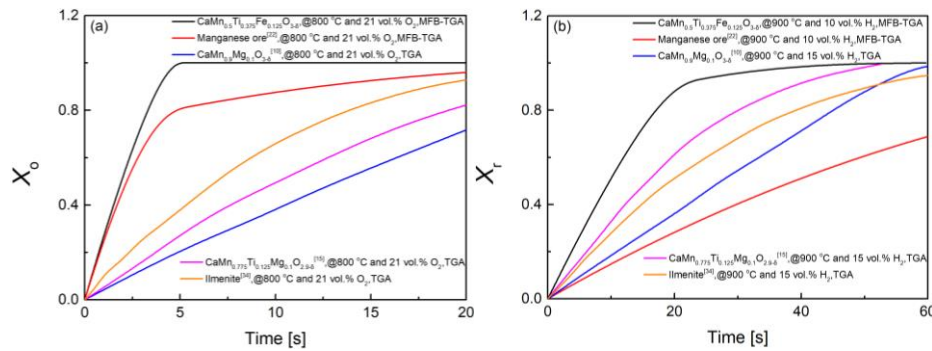

Fig. 20. Comparison of the (a) oxidization and (b) reduction kinetics for different OCMs

6. Conclusion

The oxygen uncoupling and redox kinetics of a newly developed perovskite oxide, $CaMn_{0.5}Ti_{0.375}Fe_{0.125}O_{3-\delta}$, as oxygen carrier material (OCM), was determined using a micro-fluidized bed thermogravimetric analysis apparatus (MFB-TGA). A two-stage reaction kinetic

model coupled with a simplified K-L model for the fluidized bed was used to determine oxygen uncoupling and redox kinetic parameters. The OCM shows good fluidization performance and excellent stability for more than 20 redox cycles. The rate of oxygen uncoupling is enhanced with the temperature from 800 °C to 930 °C. The initial stage of oxygen uncoupling reaction is faster when measured by the MFB-TGA, comparing the result obtained by the conventional TGA Q500. The activation energies of the first and second stages ($-E_{chem}$ and $-E_{diff}$) are 12.36 kJ mol^{-1} and 45.12 kJ mol^{-1}, respectively. The oxidation is only controlled by chemical reaction mechanism, resulting in an ultrafast reaction rate. The full oxidation can be finished within 5 s in the range of 700-900 °C. Kinetics for the reduction reaction by 10 % vol.% H_2 and 10 % vol.% CH_4 is mainly controlled by the chemical reaction during the period of low conversion level. However, a slow reaction stage controlled by gas diffusion occurs as the conversion level increased. The activation energies for reaction with 21 % vol.% O_2, 10 % vol.% H_2 and 10 % vol.% CH_4 controlled by chemical reaction stage are 18.77 kJ/mol, 27.62 kJ/mol and 72.67 kJ/mol, respectively. The SEM-EDS results show the cracks and micropores appear inside the tested particles, and the constituting elements are homogeneously distributed within the grains prior to and after redox cycles. The comparison with the mainstream OCMs shows $CaMn_{0.5}Ti_{0.375}Fe_{0.125}O_{3-\delta}$ has faster oxygen uncoupling and redox kinetics.

Acknowledgements

Nomenclature

$A_{0,chem}$	pre-exponential factor of the fast reaction stage, $m^3/mol/s$
$A_{0,diff}$	pre-exponential factor of the slow reaction stage, $m^3/mol/s$
$A_{0,L}$	pre-exponential factor of the critical conversion
Ar	Archimedes number
$c_{p,OC}$	specific heat capacity of oxygen carrier, J/kg/K
$C_{b,i}$	concentration of gas i in the bubble phase, mol/m^3
$C_{e,i}$	concentration of gas i in the emulsion phase, mol/m^3
$C_{eq,i}$	equilibrium concentration of gas i, mol/m^3
d_p	diameter of the oxygen carrier particle, m
D_i	gas i molecular diffusivity, m^2/s
E_{chem}	activation energy of the fast reaction stage, kJ/mol
E_{diff}	activation energy of the slow reaction stage, kJ/mol
E_L	activation energy of the critical conversion, kJ/mol
f_a	volume fraction of oxygen carrier particles in all solid volume
H_{mf}	bed height in the bubbling bed reactor, m
I_1	ratio of the external mass transfer rate to the reaction rate
I_2	ratio of the reaction rate in the emulsion phase to the mass transfer rate between the bubble phase and emulsion phase
k_{chem}	reaction rate constant of the fast reaction stage, $m^3/mol/s$
k_{diff}	reaction rate constant of the slow reaction stage, $m^3/mol/s$
k_g	external mass transfer coefficient, m/s

K_{be} interchange coefficient between the bubble and emulsion phase, s^{-1}

K_r reaction rate constant of particles in the emulsion phase, s^{-1}

K_{ri} reaction rate constant of particles, s^{-1}

$m(t)$ mass measured by the weight transducer at time t, g

m_o whole mass of the reactor and oxidized oxygen carrier samples, g

m_{OC} mass of the added oxygen carrier samples, g

m_r whole mass of the reactor and reduced oxygen carrier, g

M_i molar mass of i, kg/mol

R_e Reynolds number

R_g ideal gases constant, J/mol/K

$R_{OC,ou}$ oxygen transport capacity for oxygen uncoupling, wt.%

$R_{OC,t}$ total oxygen transport capacity, wt.%

Sh Sherwood number

T temperature in Kelvin, K

U_0 superficial gas velocity, m/s

U_b bubble rise velocity, m/s

U_b^* effective gas velocity in the bubble phase, m/s

U_{mf} minimum fluidization velocity, m/s

X conversion level of oxidation or reduction reaction at time t

X_{chem} conversion level of the fast reaction stage at time t

X_{diff} conversion level of the slow reaction stage at time t

X_e equilibrium conversion level of an oxygen carrier

X_o	conversion level of oxidation reaction at time t
X_{ou}	conversion level of oxygen uncoupling reaction at time t
X_r	conversion level of reduction reaction at time t
α	stoichiometric coefficient
ρ_s	particle density of oxygen carrier, kg/m^3
ε_{mf}	voidage of fluidized bed
θ	fraction of the bubble phase
δ	amount of lattice oxygen
γ	amount of lattice oxygen
ψ	ratio of the conversion level at the fast reaction stage to the conversion level

References

[1] M. Ishida, D. Zheng, T. Akehata, Evaluation of a chemical-looping-combustion power-generation system by graphic exergy analysis, Energy 12(2) (1987) 147-154.

[2] T. Mattisson, A. Lyngfelt, H. Leion, Chemical-looping with oxygen uncoupling for combustion of solid fuels, Int J Greenhouse Gas Control 3 (2009) 9-11.

[3] J. Adanez, A. Abad, F. Garcia-Labiano, P. Gayan, F. Luis, Progress in chemical-looping combustion and reforming technologies, Prog. Energ. Combust. 38(2) (2012) 215-282.

[4] W. Hu, F. Donat, S. A. Scott, J. S. Dennis, Kinetics of oxygen uncoupling of a copper based oxygen carrier, Appl. Energy 161(2016) 92-100.

[5] E. Alonso, C. Hutter, M. Romero, A. Steinfeld, J. Gonzalez-Aguilar, Kinetics of Mn_2O_3-Mn_3O_4 and Mn_3O_4-MnO Redox reactions performed under concentrated thermal radiative flux, Energy

Fuels 27 (2013) 4884-4890.

[6] P. Cho, T. Mattisson, A. Lyngfelt, Comparison of iron-, nickel-, copper-and manganese-based oxygen carriers for chemical-looping combustion, Fuel 83(9) (2004) 1215-1225.

[7] A. Abad, I. Adanez-Rubio, P. Gayan, F. García-Labiano, L. F. de′Diego, J. Adanez, Demonstration of chemical-looping with oxygen′uncoupling (CLOU) process in a 1.5 kWth continuously operating unit using a Cu-based oxygen-carrier, Int. J. Greenhouse Gas Control 6 (2012) 189-200.

[8] E.I. Leonidova, I.A. Leonidov, M.V. Patrakeev, V.L. Kozhevnikov, Oxygen non-stoichiometry, high-temperature properties, and phase diagram of $CaMnO_{3-\delta}$, J. Solid State Electrochem. 15 (2011) 1071-1075.

[9] H. Leion, Y. Larring, E. Bakken, R. Bredesen, T. Mattisson, A. Lyngfelt, Use of $CaMn_{0.875}Ti_{0.125}O_3$ as Oxygen Carrier in Chemical Looping with Oxygen Uncoupling, Energy Fuels 23 (2009) 5276-5283.

[10] L. F. de Diego, A. Abad, A. Cabello, P. Gayán, F. García-Labiano, J. Adánez, Reduction and oxidation kinetics of a $CaMn_{0.9}Mg_{0.1}O_{3-\delta}$ oxygen carrier for chemical-looping combustion, Ind. Eng. Chem. Res. 53(1) (2013) 87-103.

[11] M. Arjmand, A. Hedayati, A.M. Azad, H. Leion, M. Rydén, T. Mattisson, $Ca_xLa_{1-x}Mn_{1-y}M_yO_{3-\delta}$ (M = Mg, Ti, Fe, or Cu) as Oxygen Carriers for Chemical-Looping with Oxygen Uncoupling (CLOU), Energy Fuels 27 (2013) 4097-4107.

[12] R. Ruhl, J. Song, V. Thoreton, S. P. Singh, K. Wiik, Y. Larring, H. J. Bouwmeester, Structure, electrical conductivity and oxygen transport properties of perovskite-type oxides $CaMn_{1-x-y}Ti_xFe_yO_{3-\delta}$, Phys. Chem. Chem. Phys. (2019).

[13] W. Xing, M. L. Fontaine, Z. Li, J. MPolfus, Y. Larring, CDenonville, R. Bredesen, Asymmetric tubular $CaTi_{0.6}Fe_{0.15}Mn_{0.25}O_{3-\delta}$ membranes: Membrane architecture and long-term stability, J. Membrane Sci. 548 (2018) 372-379.

[14] F. García-Labiano, L.F. de Diego, J. Adánez, A. Abad, P. Gayán, Reduction and oxidation kinetics of a copper-based oxygen carrier prepared by impregnation for chemical-looping combustion, Ind. Eng. Chem. Res. 43 (2004) 8168-8177.

[15] A. Abad, A. Cabello, P. Gayán, F. García-Labiano, L. F. de Diego, T. Mendiara, J. Adánez, Kinetics of $CaMn_{0.775}Ti_{0.125}Mg_{0.1}O_{2.9-\delta}$ perovskite prepared at industrial scale and its implication on the performance of chemical looping combustion of methane, Chem. Eng. J. (2020) 124863. Accepted.

[16] C. K. Clayton, K. J. Whitty, Measurement and modeling of decomposition kinetics for copper oxide-based chemical looping with oxygen uncoupling, Appl. Energy 116 (2014) 416-423.

[17] B. Stanmore, P. Gilot, G. Prado, The influence of mass transfer in DTG combustion tests, Thermochim. Acta 240 (1994) 79-89.

[18] S. Y. Chuang, J. S. Dennis, A. N. Hayhurst, S. A. Scott, Kinetics of the Oxidation of a Co-precipitated Mixture of Cu and Al_2O_3 by O_2 for Chemical-Looping Combustion, Energy Fuels 24 (2010) 3917-3927.

[19] S. Y. Chuang, J. S. Dennis, A. N. Hayhurst, S. A. Scott, Kinetics of the chemical looping oxidation of H_2 by a co-precipitated mixture of CuO and Al_2O_3, Chem. Eng. Res. Des. 89(9) (2011) 1511-1523.

[20] P. S. Fennell, S. Kadchha, H. Y. Lee, J. S. Dennis, A. N. Hayhurst, The measurement of the rate of burning of different coal chars in an electrically heated fluidised bed of sand, Chem. Eng. Sci.

62(1-2) (2007) 608-618.

[21] Y. Li, Z. Li, L. Liu, N. Cai, Measuring the fast oxidation kinetics of a manganese oxygen carrier using microfluidized bed thermogravimetric analysis, Chem. Eng. J. 385 (2020) 123970.

[22] L. Liu, Z. Li, Z. Li, Y. Larring, Y. Li, N. Cai, Fast redox kinetics of a perovskite oxygen carrier measured using micro-fluidized bed thermogravimetric analysis, Proc. Combust. Inst. (2020).

[23] Y. Li, H. Wang, W. Li, Z. Li, N. Cai, CO_2 Gasification of a Lignite Char in Microfluidized Bed Thermogravimetric Analysis for Chemical Looping Combustion and Chemical Looping with Oxygen Uncoupling, Energy fuels 33(1) (2018) 449-459.

[24] Y. Li, Z. Li, H. Wang, N. Cai, CaO carbonation kinetics determined using micro-fluidized bed thermogravimetric analysis, Fuel 264 (2020) 116823.

[25] H. Bi, Regime transitions in gas-solid circulating fluidized beds, AIChE Meeting, Los Angeles, 1991.

[26] D. Kunii, O. Levenspiel, Fluidization Engineering, Butterworth-Heinemann, Newton, U.S.A. ,1991, p. 155.

[27] J. Bao, Z. Li, N. Cai, Reduction Kinetics of Foreign-Ion-Promoted Ilmenite Using Carbon Monoxide (CO) for Chemical Looping Combustion, Ind. Eng. Chem. Res. 52(2013) 10646-10655.

[28] H. Wang, Z. Li, N. Cai, A Multiscale Model of Oxidation Kinetics for Cu-Based Oxygen Carrier in Chemical Looping with Oxygen Uncoupling, Materials 12 (2019) 1170.

[29] F. García-Labiano, F. Luis, J. Adánez, A. Abad, P. Gayán, Temperature variations in the oxygen carrier particles during their reduction and oxidation in a chemical-looping combustion system, Chem. Eng. Sci. 60(2005) 851-862.

[30] J. Bao, Z. Li, H. Sun, N. Cai, Experiment and rate equation modeling of Fe oxidation kinetics

in chemical looping combustion, Combust. Flame 160(2013) 808-817.

[31] Z. Li, General rate equation theory for gas-solid reaction kinetics and its application to CaO carbonation, Chem. Eng. Sci. 227(2020) 115902.

[32] S. Ergun, Fluid flow through packed columns, Chem. Eng. Prog. 48(1952) 89-94.

[33] J. C. Abanades, E. J. Anthony, D. Y. Lu, C. Salvador, D. Alvarez, Capture of CO_2 from 10 combustion gases in a fluidized bed of CaO, AIChE Journal 50(2004) 1614-1622.

[34] A. Abad, J. Adánez, A. Cuadrat, F. García-Labiano, P. Gayán, L.F. de Diego, Kinetics of redox reactions of ilmenite for chemical-looping combustion, Chem. Eng. Sci. 66 (2011) 689-702.

[35] T. Mendiara, A. Abad, L.F. de Diego, F. García-Labiano, P. Gayán, J. Adánez, Reduction and oxidation kinetics of Tierga iron ore for Chemical Looping Combustion with diverse fuels, Chem. Eng. J. 359 (2019) 37-46.

[36] A. Abad, J. Adánez, F. García-Labiano, L.F. de Diego, P. Gayán, J. Celaya, Mapping of the range of operational conditions for Cu-, Fe-, and Ni-based oxygen carriers in chemical-looping combustion, Chem. Eng. Sci. 62 (2007) 533-549.

[37] I. Adánez-Rubio, P. Gayán, A. Abad, F. García-Labiano, L. F. De Diego, J. Adánez, Kinetic analysis of a Cu-based oxygen carrier: Relevance of temperature and oxygen partial pressure on reduction and oxidation reactions rates in Chemical Looping with Oxygen Uncoupling (CLOU), Chem. Eng. J. 256(2014) 69-84.